nature research

https://doi.org/10.1038/s41560-020-00757-7

Supplementary information

Thermally modulated lithium iron phosphate batteries for mass-market electric vehicles

In the format provided by the authors and unedited

natureresearch

https://doi.org/10.1038/s41560-020-00757-7

Supplementary information

Thermally modulated lithium iron phosphate batteries for mass-market electric vehicles

In the format provided by the authors and unedited

Supplementary Information for

Thermally Modulated Lithium Iron Phosphate Batteries for Mass-Market Electric Vehicles

Xiao-Guang Yang[1], Teng Liu[1], and Chao-Yang Wang[1,2,*]

[1] Department of Mechanical Engineering and Electrochemical Engine Center (ECEC), The Pennsylvania State University, University Park, Pennsylvania 16802, USA.

[2] EC Power, 341 Science Park Road, State College, Pennsylvania 16803, USA.

[*]Corresponding author. Email: cxw31@psu.edu

This file includes:

Supplementary Table 1| Specific energy and energy density of commercial EV batteries at pack and cell levels.

Supplementary Table 2| Design information of the blade-type LFP cell and prismatic-type NMC622 cell (VDA-BEV2 standard) studied in this work.

Supplementary Fig. 1| Validation of the ECT model for predicting C-rates effects on graphite-NMC622 cells.

Supplementary Fig. 2| Validation of the ECT model for predicting temperature effects on graphite-NMC622 cells.

Supplementary Fig. 3| Validation of the ECT model for predicting C-rates effects on graphite-LFP cells.

Supplementary Fig. 4| Validation of the ECT model for predicting temperature effects on graphite-LFP cells.

Supplementary Fig. 5| Peak specific power of the LFP blade cells and NMC622 VDA cells.

Supplementary Fig. 6| Peak power density of the LFP blade cells and NMC622 VDA cells.

Supplementary Fig. 7| City and highway driving profiles.

Supplementary Fig. 8| Thicker LFP cathode leads to larger mass-transfer resistance.

Supplementary Fig. 9| Li plating induced by regenerative braking at freezing temperatures.

Supplementary Fig. 10| Temperature effects on the maximum charge rate of the LFP and NMC622 cells.

Supplementary Fig. 11| Elevated temperature accelerates all electrochemical and transport processes.

Supplementary Fig. 12| All-climate cruise range with TM-LFP battery.

Supplementary Fig. 13| Validation of the aging model for the graphite-LFP cell.

Supplementary Fig. 14| Cell performance is insensitive to graphite BET area at the elevated temperature of 60^{o}C.

Supplementary Note 1| Voltage loss along length of current collectors.

Supplementary Table 1| Summary of the specific energy and energy density of commercial EV batteries at pack and cell levels.

	Pack-Level					**Cell-level**						**CTP Ratios**	
OEM and Model	Energy (kWh)	Weight (kg)	Volume (L)	Specific Energy (Wh/kg)	Energy Density (Wh/L)	Capacity (Ah)	Nominal Voltage (V)[a]	Weight (kg)	Volume (L)	Specific Energy (Wh/kg)	Energy Density (Wh/L)	GCTP	VCTP
Tesla Model 3 LR (2017)	75[1]	457[1]	314[1]	164	239	4.8[2]	3.65	0.0685[2]	0.02425[2]	256	722	0.64	0.33
BMW i3 (2018)	33[3]	256[3]	278.4[4]	129	119	94[2]	3.65	2.02[2]	0.973[2]	170	353	0.76	0.34
BMW i3 (2019)	42.2[3]	278[3]	278.4[4]	152	152	120[2]	3.65	2.25[b]	0.973[2]	195	450	0.78	0.34
Nissan Leaf (2019)	40[5]	303[5]	485[5]	132	82	56.3[6]	3.65	0.916	0.447	224[6]	460[6]	0.59	0.18
Chevy Bolt (2018)	60[1]	435[1]	306[1]	138	196	60[2]	3.65	0.835[2]	0.398[2]	262	550	0.53	0.36
Renault ZOE ZE40 (2018)	44.1[3]	305[3]	N/A	145	N/A	65.6[7]	3.65	0.965[7]	0.467[7]	248	513	0.58	N/A
Renault ZOE ZE50 (2019)	54.7[8]	326[8]	N/A	168	N/A	78[8]	3.65	1.073[8]	N/A	265	N/A	0.63	N/A
Audi E-tron (2018)	95[9]	681[9]	1238[9]	140	77	60[c]	3.65	0.86[c]	0.432[c]	255	507	0.55	0.15
Hyundai Kona 2018	64[1]	452[1]	390[1]	142	164	60[1]	3.65	0.86[1]	0.432[1]	255	507	0.56	0.32
Jaguar I-PACE (2019)	90.2[10]	610[10]	472[10]	148	191	58[10]	3.65	0.815[10]	0.384[10]	260	551	0.57	0.35
Mercedes EQC (2019)	85[3]	652[3]	N/A	130	N/A	63[11]	3.65	0.965[11]	0.467[11]	238	492	0.55	N/A
NIO ES8 (2018)	72.8[9]	525[9]	432[9]	139	169	50[11]	3.65	0.81[11]	0.35[11]	225	521	0.62	0.32
Hyundai IONIQ	40.4[3]	359[3]	N/A	113	N/A	65.6[7]	3.65	0.965[7]	0.467[7]	248	513	0.45	N/A
BYD Han	65.9[12]	471[12]	238[12]	140	277	202[13]	3.2	3.91[13]	1.442[13]	165[12]	448	0.85	0.62

[a] For all NMC/NCA cells, we use nominal voltage of 3.65V to calculate cell energy.

[b] Estimated by assuming that the increased battery-pack weight from 2018 version to 2019 version all comes from cells (i.e., the same overall mass of inert parts such as metal cans, cabling, BMS, etc.). Thus, the total cell weight increase from 194kg in 2018 version to 216kg in 2019 version. Each pack has 96 cells.

[c] Estimated based on the specifications of LG Chem E63B pouch cells.

Supplementary Table 2| Design information of the blade-type LFP cell and prismatic-type NMC622 cell (VDA-BEV2 standard) studied in this work.

		VDA-BEV2 NMC622 cell	**Blade-type LFP cell**
Anode	Active material	Graphite	Graphite
	Areal capacity	3.3 mAh/cm^2	3.3 mAh/cm^2
	Porosity	0.27	0.27
	Single-side thickness	56.8 μm	56.8 μm
	Cu foil thickness	8 μm	8 μm
	Dimension	115×166 mm	110×885 mm
	Number of layers	160	39
Cathode	Active material	$LiNi_{0.6}Mn_{0.2}Co_{0.2}O_2$	$LiFePO_4$
	Areal capacity	3.0 mAh/cm^2	3.0 mAh/cm^2
	Porosity	0.27	0.27
	Single-side thickness	47.4 μm	75.6 μm
	Al foil thickness	13 μm	13 μm
	Dimension	112×163 mm	108×883 mm
	Number of layers	159	38
Electrolyte	1M $LiPF_6$ dissolved in EC/EMC (3:7 by wt.)+2wt% VC		
Separator	20 μm thick, porosity 0.4		
Dimension		125×173×45 mm	118×905×13.5 mm
Weight		2296.4 g	3493.7 g
Capacity		158 Ah	202 Ah

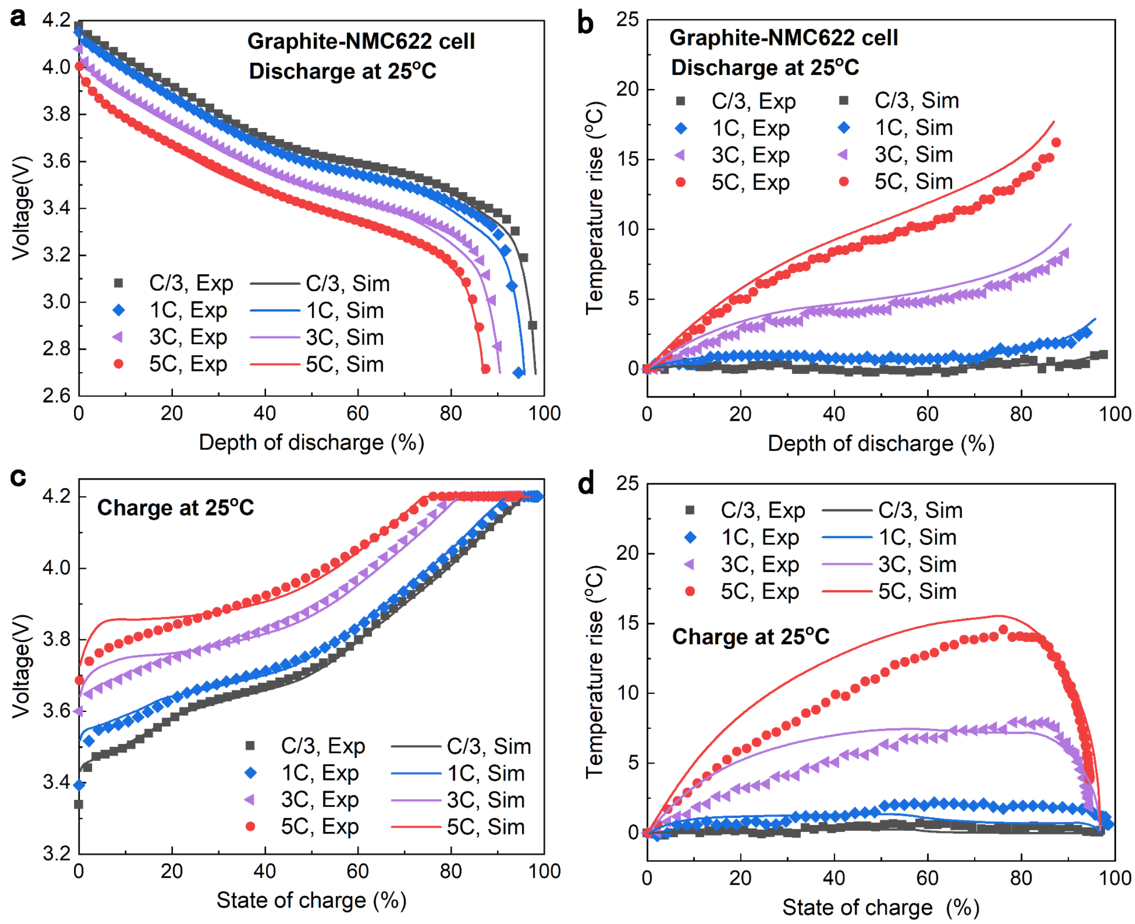

Supplementary Fig. 1| Validation of the ECT model for predicting C-rates effects on graphite-NMC622 cells. Comparison of modeling results with the experimental data in Ref.[14] for **(a,b)** discharge and **(c,d)** charge of a 10-Ah graphite-NMC622 pouch cell with various C-rates at the ambient temperature of 25°C.

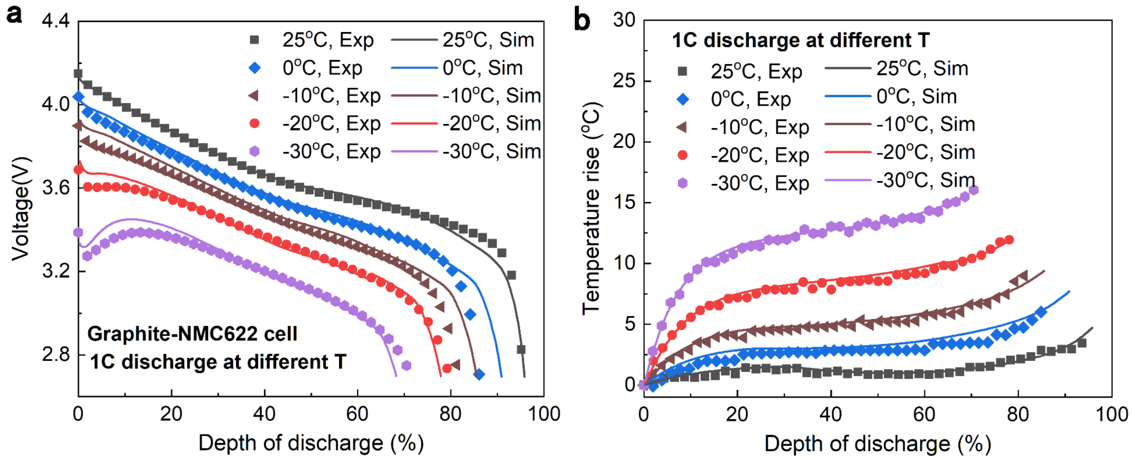

Supplementary Fig. 2| Validation of the ECT model for predicting temperature effects on graphite-NMC622 cells. Comparison of modeling results with the experimental data in Ref.[14] for 1C discharge of a 10-Ah graphite-NMC622 pouch cell at different ambient temperatures.

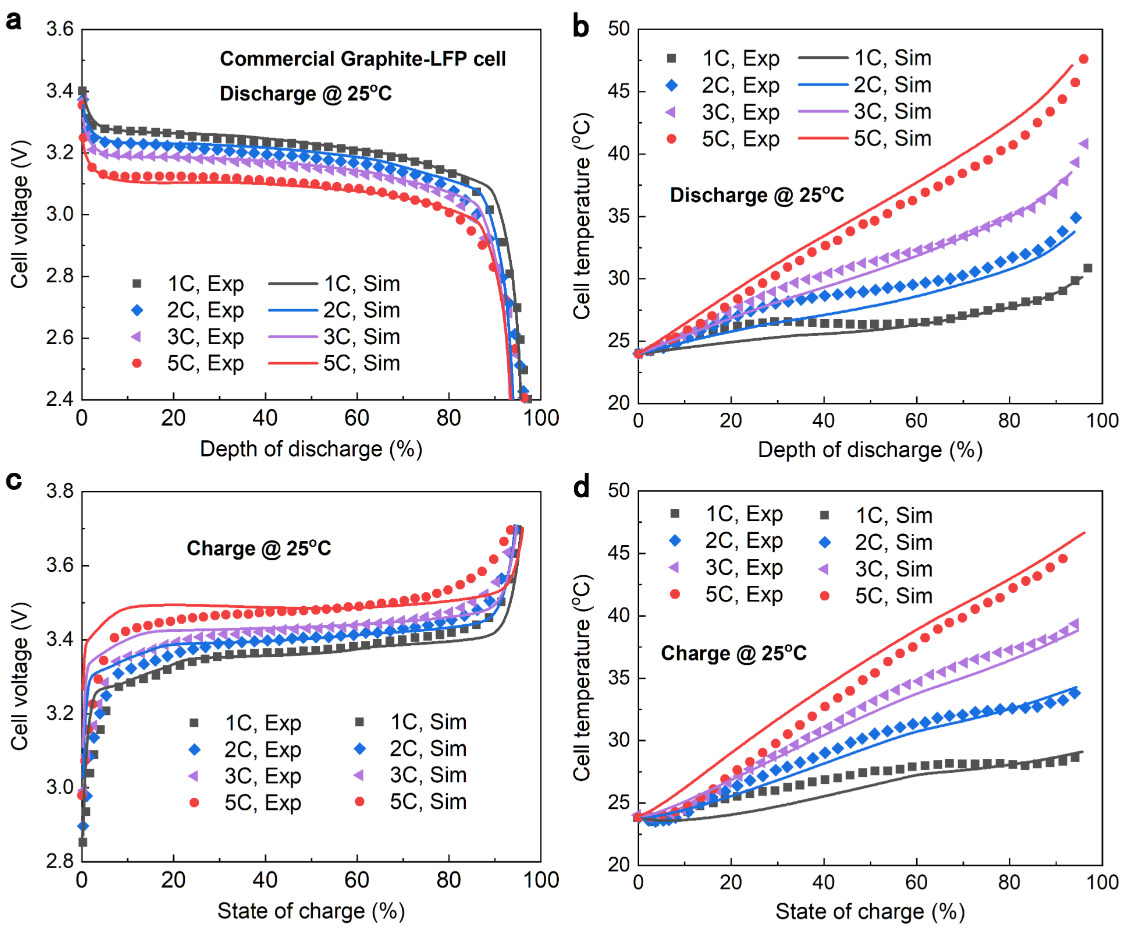

Supplementary Fig. 3| Validation of the ECT model for predicting C-rates effects on graphite-LFP cells. Comparison of modeling results with the experimental data in Refs.[15, 16] for **(a,b)** discharge and **(c,d)** charge of a 20-Ah graphite-LFP commercial cell (from A123) at the ambient temperature of 25°C.

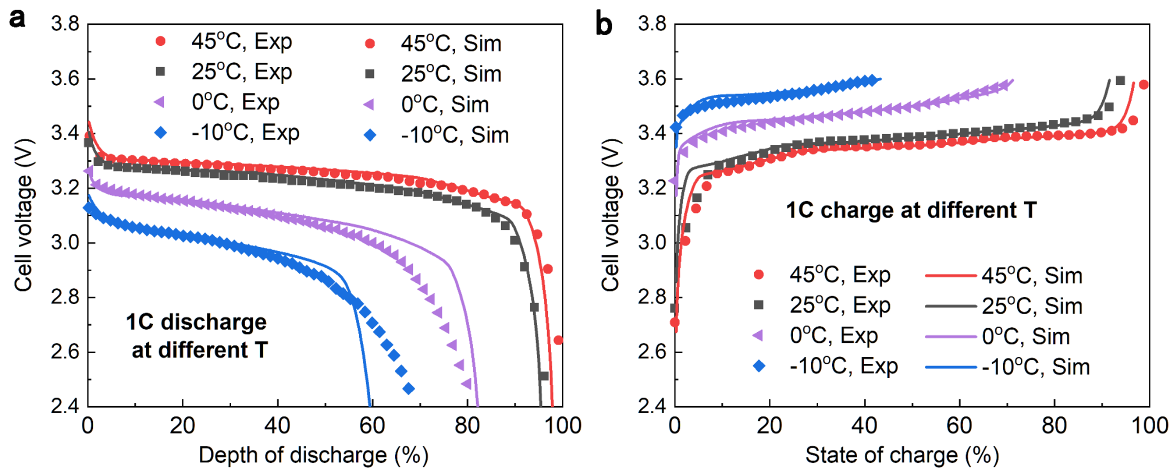

Supplementary Fig. 4| Validation of the ECT model for predicting temperature effects on graphite-LFP cells. Comparison of modeling results with the experimental data in Ref.[17] for **(a)** discharge and **(b)** charge with 1C rate at different ambient temperatures.

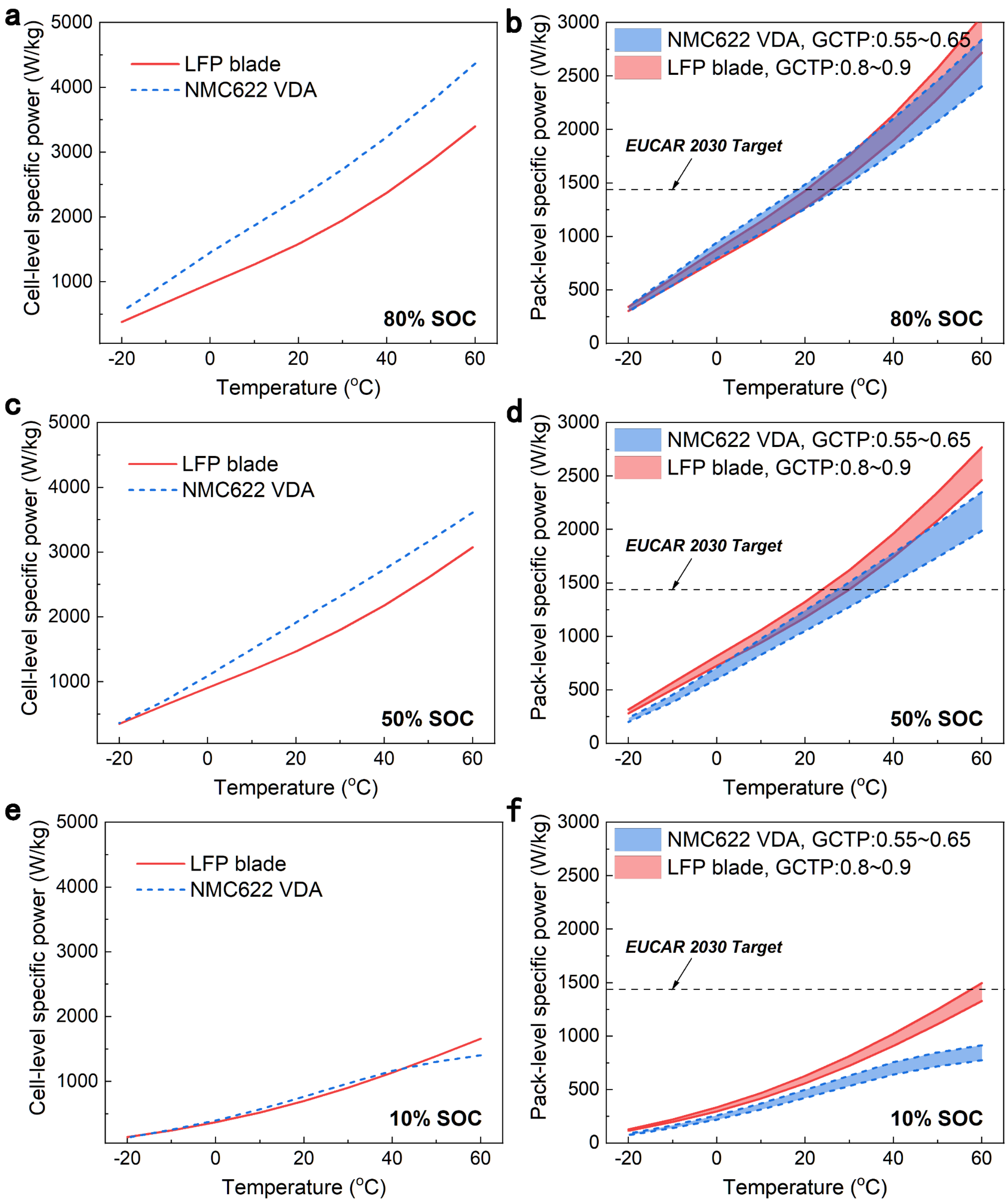

Supplementary Fig. 5| Peak specific power of the LFP blade cells and NMC622 VDA cells. Comparison of the peak specific power of the LFP blade battery and NMC622 prismatic battery (VDA-BEV2 standard) at **(a,b)** 80% SOC, **(c,d)** 50% SOC, and **(e,f)** 10% SOC in different temperatures. **(a,c,e)** are at the cell level, and **(b,d,f)** are at the pack level. The LFP blade battery has a higher gravimetric cell to pack ratio (GCTP) than the conventional NMC622 VDA battery. The peak power is evaluated by a 10-sec discharge at a constant voltage of 2.4V for the LFP cell and 2.7V for the NMC622 cell, which represents the maximum power the cells can deliver at a given state.

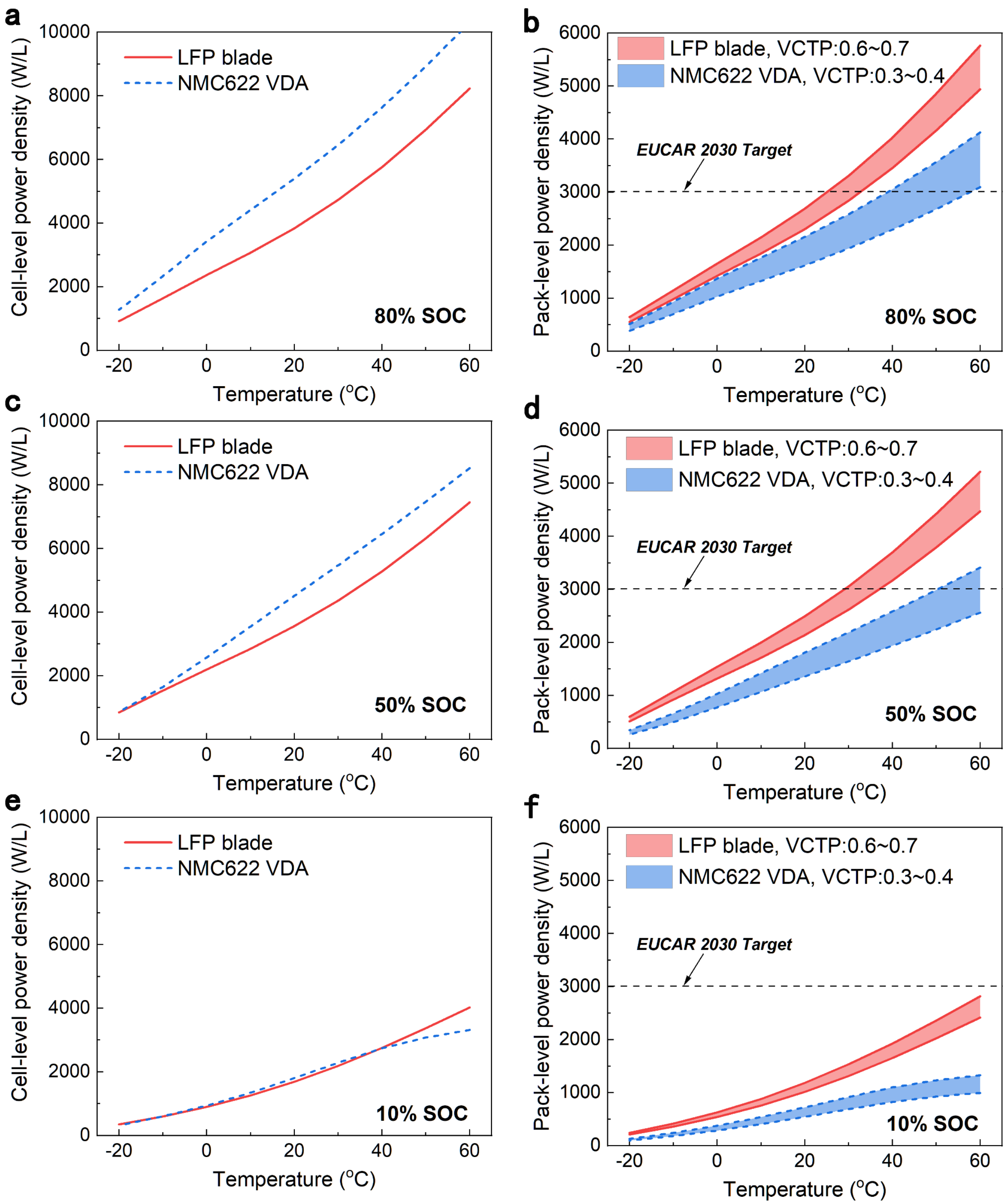

Supplementary Fig. 6| Peak power density of the LFP blade cells and NMC622 VDA cells. Comparison of the peak power density of the LFP blade battery and the NMC622 prismatic battery (VDA-BEV2 standard) at **(a,b)** 80% SOC, **(c,d)** 50% SOC, and **(e,f)** 10% SOC in different temperatures. **(a,c,e)** are at the cell level, and **(b,d,f)** are at the pack level. The LFP blade battery has a higher volumetric cell to pack ratio (VCTP) than the conventional NMC622 VDA battery.

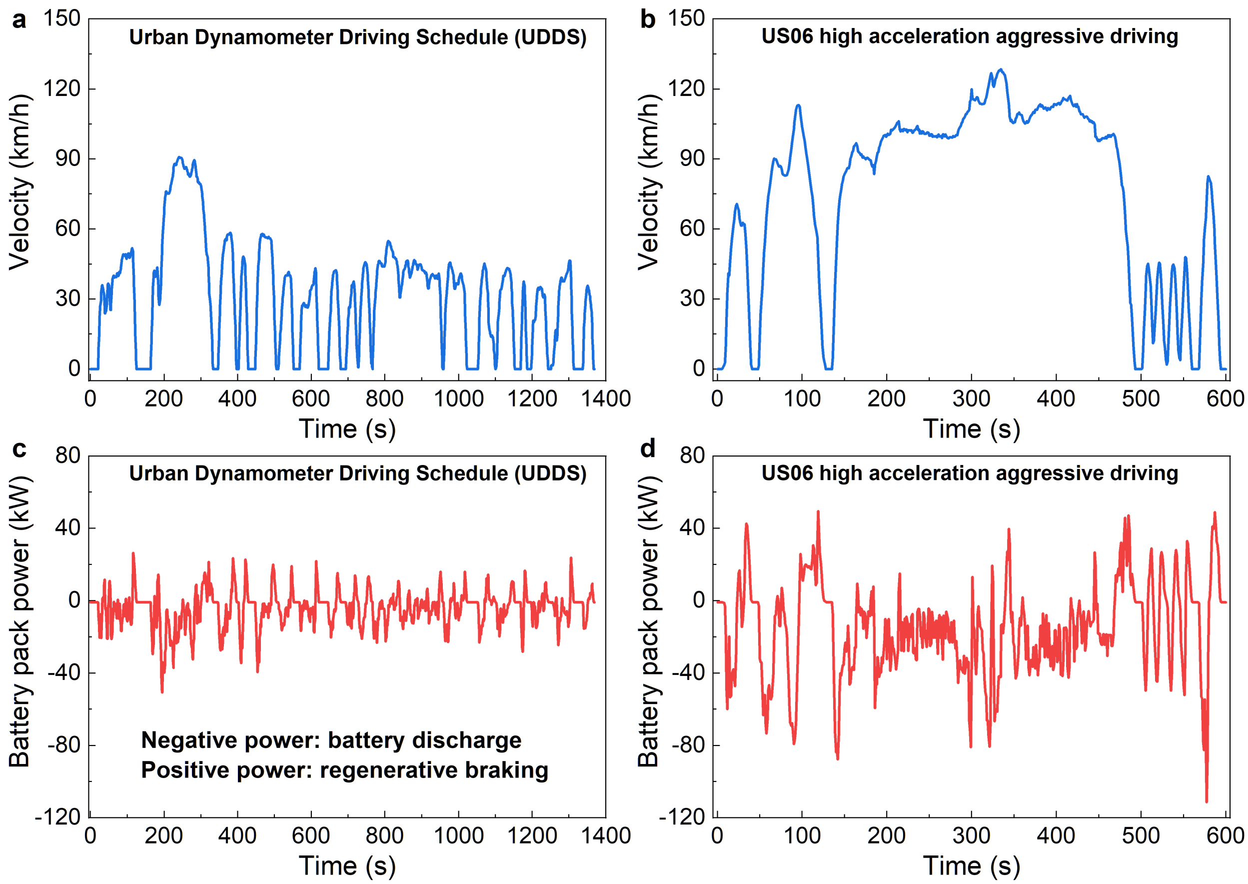

Supplementary Fig. 7| City and highway driving profiles. The profiles of **(a,b)** vehicle velocity and **(c,d)** battery pack power under the US EPA-defined driving cycles of **(a,c)** Urban Dynamometer Driving Schedule (UDDS) and **(b,d)** US06 high acceleration aggressive driving. The velocity profiles are converted to battery power profiles through a vehicle dynamics model (*see Methods*) based on the specifications of Nissan Leaf. The vehicle carries a 40kWh battery pack, which consists of either 62 of the 202Ah LFP cells or 69 of the 158Ah NMC622 cells shown in Table S2. The driving cycle is repeated until the single-cell voltage reaches the cutoff value (2.4V for the LFP cell and 2.7V for the NMC622 cell), and the driving range shown in Figs. 3 and 5 are calculated by integrating the velocity profiles over time. The cases without regenerative braking (the solid bars in Fig. 3c&d) considers only the battery discharge power (i.e., the positive values of battery power in Supplementary Fig. 7c&d are replaced with zero).

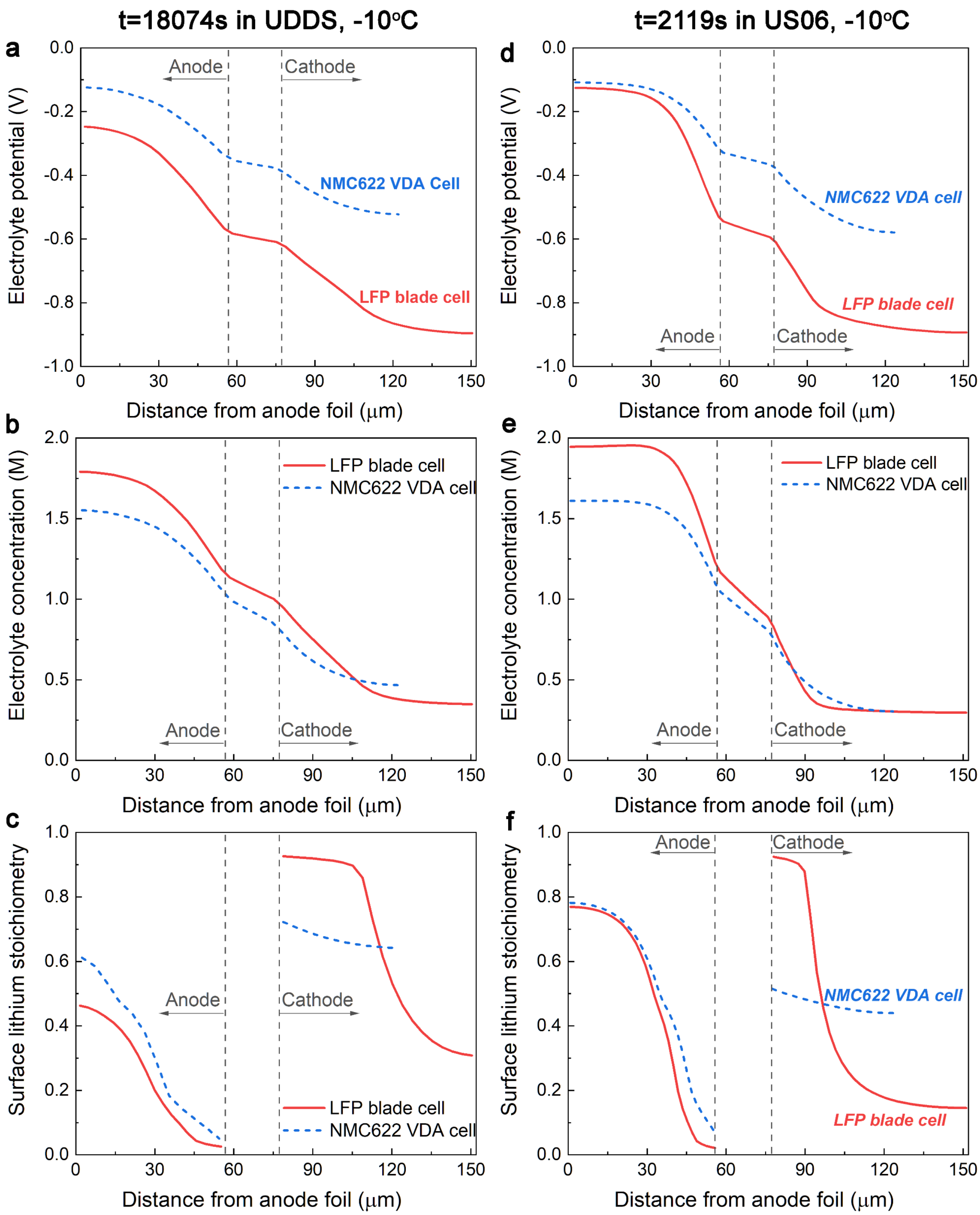

Supplementary Fig. 8| Thicker LFP cathode leads to larger mass-transfer resistance. Distributions of **(a,b)** electrolyte-phase potential, **(c,d)** electrolyte concentration, and **(e,f)** lithium surface stoichiometry across the thickness of the LFP and NMC622 cells at the time when the LFP cell reaches the 2.4V cutoff voltage during **(a-c)** UDDS and **(d-f)** US06 cycling at -10°C. The thickness of the LFP cathode is 1.6x of the thickness of the NMC622 cell at the same areal capacity of 3 mAh/cm^2.

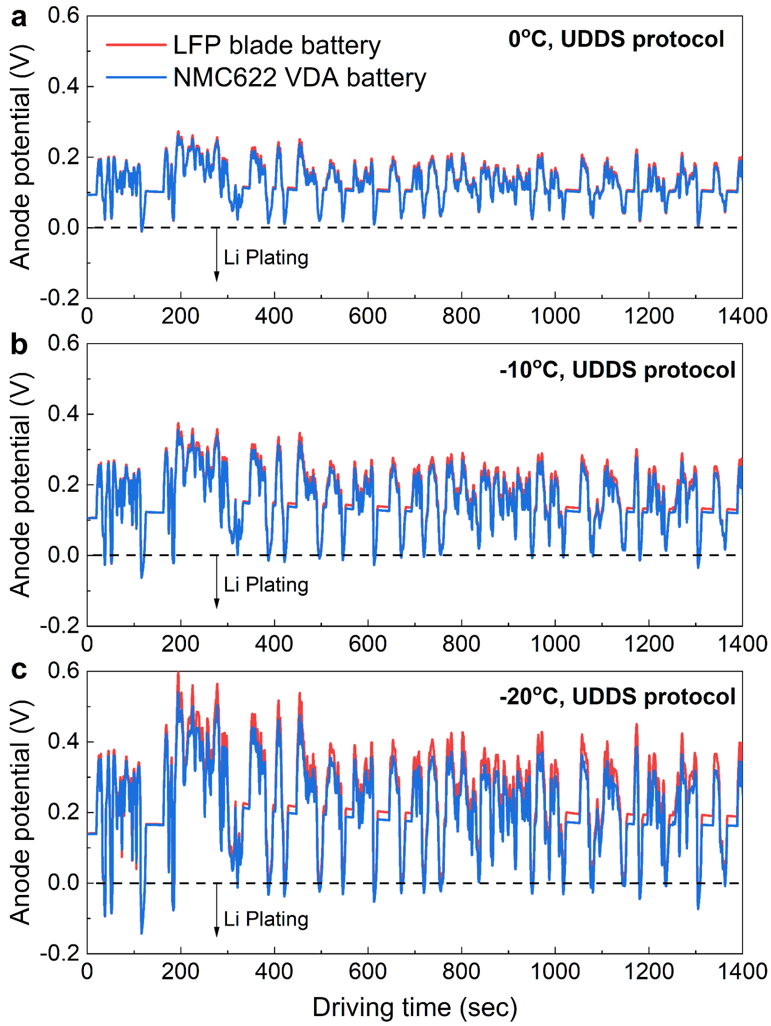

Supplementary Fig. 9| Li plating induced by regenerative braking at freezing temperatures. Evolution of the anode potential (at the anode-separator interface) in the graphite-LFP and graphite-NMC622 cells under the UDDS driving cycle at different ambient temperatures: **(a)** 0°C, **(b)** -10°C, **(c)** -20°C. Only the results in the first cycle are presented. Li plating occurs when the anode potential becomes negative.

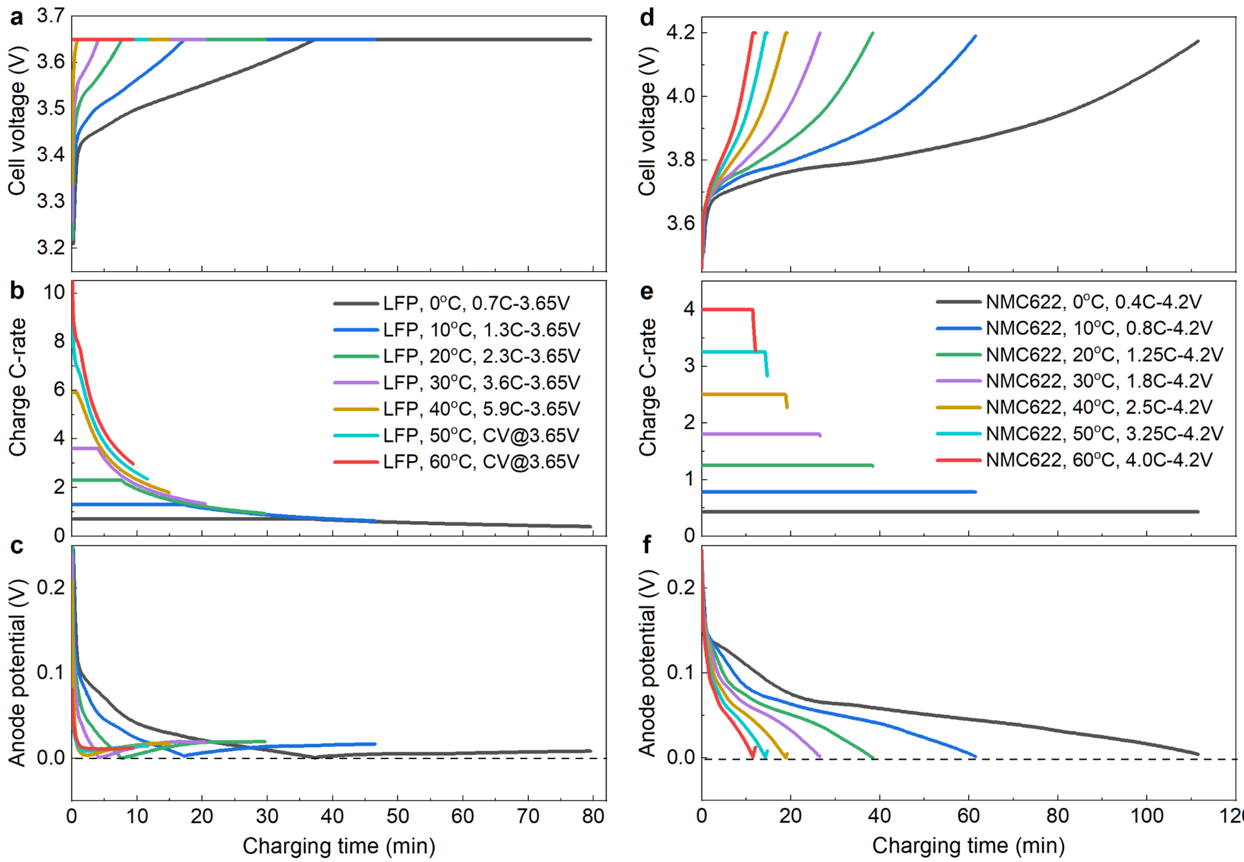

Supplementary Fig. 10| Temperature effects on the maximum charge rate of LFP and NMC622 cells. Evolutions of **(a,d)** cell voltage, **(b,e)** charge C-rate, and **(c,f)** the anode potential (at anode-separator interface) during charging of the **(a-c)** graphite-LFP and **(d-f)** graphite-NMC622 cells at the maximum charge rate without Li plating (anode potential >0V). The LFP and NMC622 cells have the same anode design: the anode areal capacity is 3.3 mAh/cm^2 (N-P ratio 1.1) and the anode porosity is 0.27.

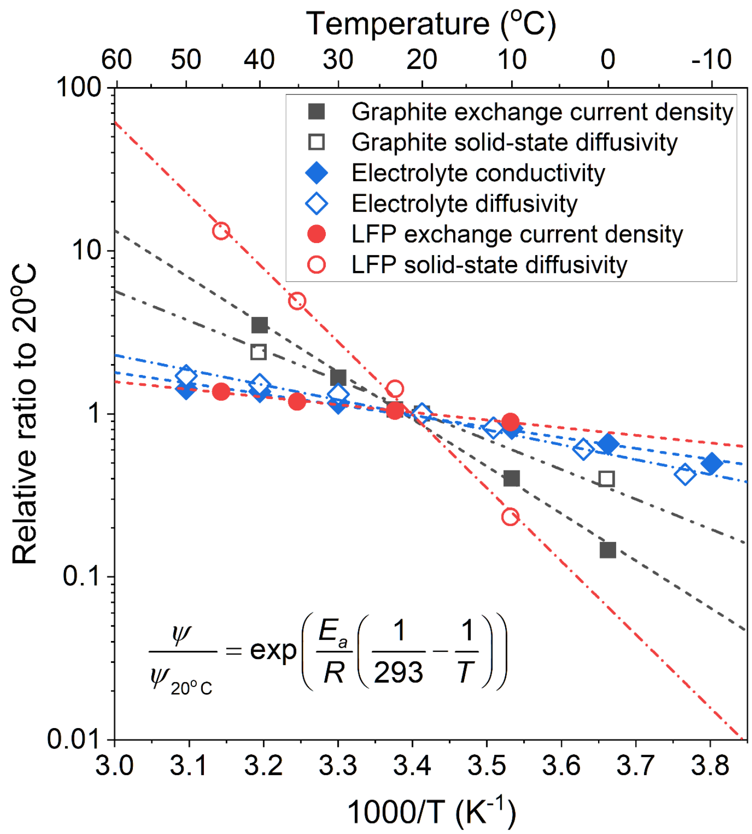

Supplementary Fig. 11| Elevated temperature accelerates all electrochemical and transport processes. Relative ratio to the value at 20ºC for graphite exchange current density[18], graphite solid-state lithium diffusivity[19], electrolyte conductivity[20], electrolyte diffusivity[20], LFP exchange current density[16], and LFP solid-state lithium diffusivity[16]. All these parameters depend on the temperature, following the Arrhenius law (the inset equation).

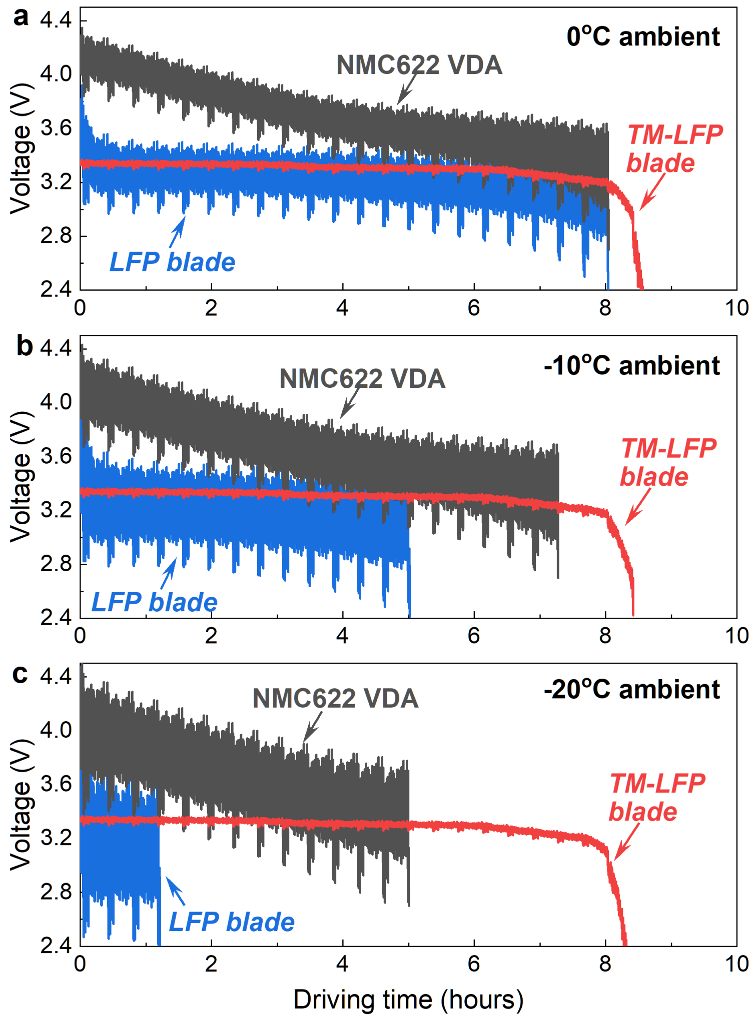

Supplementary Fig. 12| All-climate cruise range with TM-LFP battery. Evolution of single-cell voltage under the Urban Dynamometer driving schedule (UDDS) at the ambient temperature of **(a)** 0ºC, **(b)** -10ºC, and **(c)** -20ºC. Three types of cells are compared: LFP blade cells, NMC622 prismatic cells (VDA-BEV2 standard), and thermally-modulated (TM-) LFP blade cells. The regular LFP and NMC622 cells start the UDDS cycle at 100% state of charge (SOC) with their initial temperature equal to ambient temperature. The TM-LFP battery is preheated from ambient temperature to 60ºC before the UDDS cycle, and we assume 1.35% battery energy consumption per 10ºC temperature rise (e.g., the initial SOC of the TM-LFP battery is 91.9% at 0ºC ambient, 90.55% at -10ºC ambient, and 89.2% at -20ºC ambient).

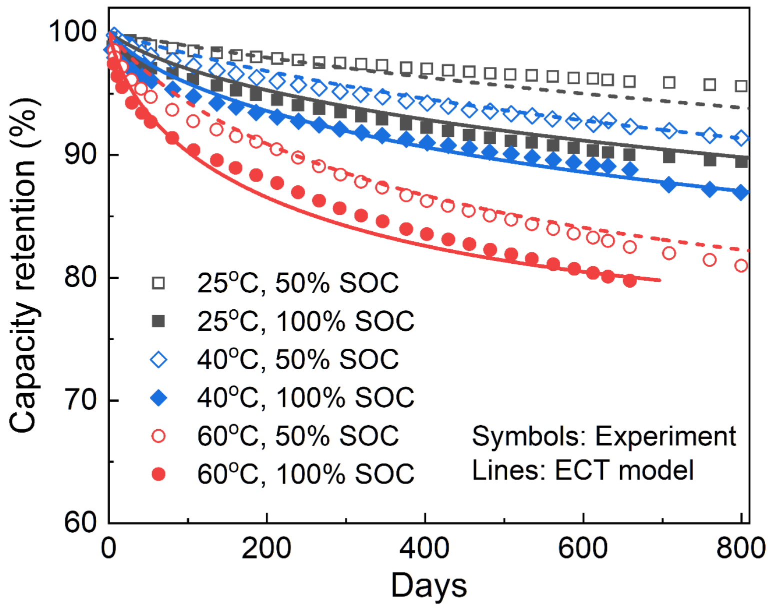

Supplementary Fig. 13| Validation of the aging model for the graphite-LFP cell. Comparison of the modeling results with experimental data on calendar aging of a graphite-LFP cell at different temperatures and state of charge (SOC). The experimental data are from Naumann et al.[21], which were based on a commercial 3 Ah graphite-LFP cell from Sony/Murata.

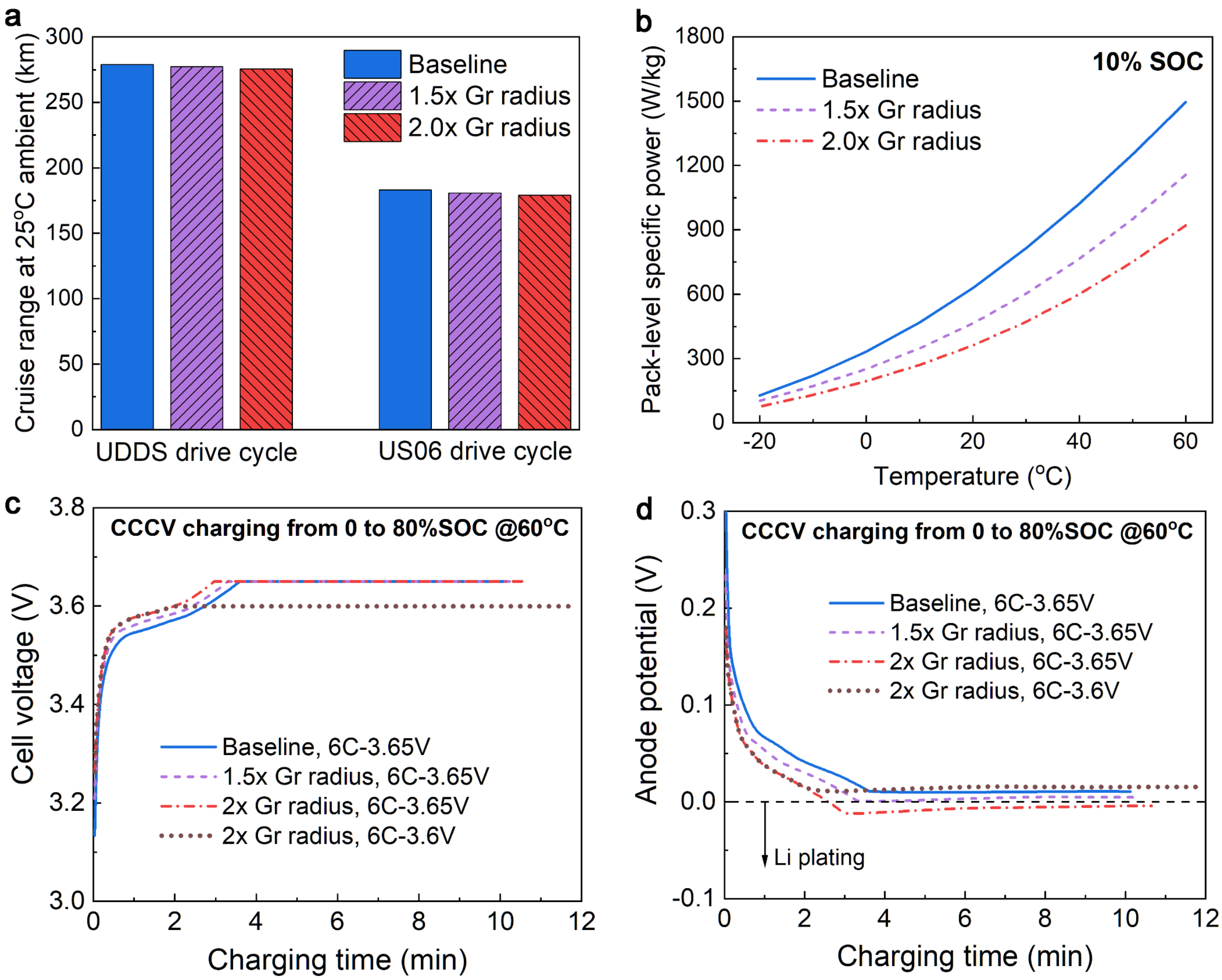

Supplementary Fig. 14| Cell performance is insensitive to graphite BET area at the elevated temperature of 60°C. Comparison of the performance of a TM-LFP blade battery with different graphite particle sizes. **(a)** Cruise range at the ambient temperature of 25°C under the UDDS and US06 driving cycle with a 40-kWh TM-LFP blade battery pack. The starting battery SOC is 95.3%, assuming a consumption of 4.7% battery energy for preheating from 25°C to 60°C before the operation. **(b)** Peak specific power of the graphite-LFP blade cell at 10% SOC. The values are at pack level, assuming a gravimetric cell to pack ratio (GCTP) of 0.9. The peak power is evaluated with a 10-sec discharge pulse at a constant voltage of 2.4V. **(c&d)** Evolutions of **(c)** cell voltage and **(d)** anode potential during charging of the graphite-LFP cell at 60°C with constant-current-constant-voltage (CCCV) protocol. The baseline cell and the cell with a 1.5x graphite radius can be safely charged (without Li plating) using a 6C rate and 3.65V cutoff voltage. The same protocol induces Li plating for the cell with a 2x graphite radius. By lowering the upper cutoff voltage to 3.6V, the cell with 2x graphite radius can be charged with 6C and yields no Li plating.

Supplementary Note 1: Voltage loss along length of current collectors

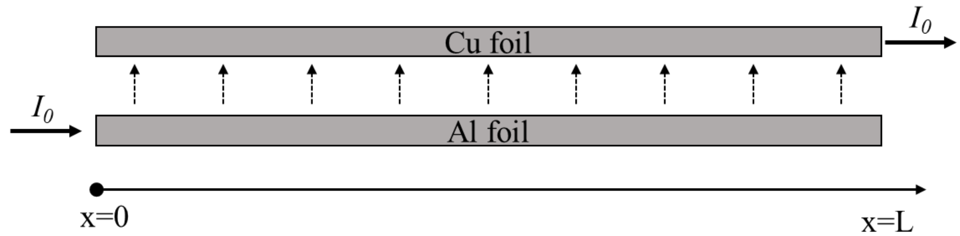

Here, we analyze the voltage loss induced by electrons transfer along the anode and cathode foils of a blade-type cell. As sketched above, we assume that the current (in charging) flows into the aluminum foil at x=0 and flows out through the copper (Cu) foil at x=L. Since $\sigma_{Al}\delta_{Al} \approx \sigma_{Cu}\delta_{Cu}$, where σ is electronic conductivity and δ is foil thickness, we can assume a uniform distribution of the reaction current along the x-direction:

$$\begin{aligned} &\frac{d}{dx} I_{Al}(x) = -\frac{d}{dx} I_{Cu}(x) = -\frac{I_0}{L} \\ &I_{Al}\big|_{x=0} = I_0, \; I_{Al}\big|_{x=L} = 0 \\ &I_{Cu}\big|_{x=0} = 0, \; I_{Cu}\big|_{x=L} = I_0 \end{aligned} \tag{S1}$$

Then we can get the current in the Al and Cu foils:

$$I_{Al}(x) = (1 - \frac{x}{L}) I_0 \qquad I_{Cu}(x) = \frac{x}{L} I_0 \tag{S2}$$

If the cell has a single-side areal capacity of q (Ah/m^2) and the charge C-rate is n, the current I_0 can be calculated as:

$$I_0 = 2nqbL \tag{S3}$$

where b is the foil width. As the voltage drop across the Al or Cu foil is the same, we calculate the voltage loss along the length of Al foil, as:

$$\Delta V = \int_0^L \frac{1}{\sigma_{Al}} \frac{I_o}{\delta_{Al} b} (1 - \frac{x}{L}) dx = \frac{I_o L}{2\sigma_{Al}\delta_{Al} b} = \frac{nqL^2}{\sigma_{Al}\delta_{Al}} \tag{S4}$$

For a cell with L=1 m, areal capacity q=30Ah/m^2, σ_{Al}=3.5×10^7 S/m, δ=13×10^{-6} m, a 6C charge results in a voltage difference of 0.4V. Thus, it is vitally important to have multi-tab design or "tab everywhere" design in order to reduce the electron-flow length and minimize the voltage spatial difference to say <10mV.

Supplementary References

1. Vishwasr, R. Continued Glimpses into xEV Batteries on the Market – AVL Series Battery Benchmarking: *AVL* (2019)
2. Hummel, P., Bush, T., Gong, P., Yasui, K., Lee, T., Radlinger, J., *et al.* Tearing down the heart of an electric car: Can batteries provide an edge, and who wins?: *UBS Evidence Lab* (November 18, 2018)
3. Comparison of different EV batteries in 2020. https://pushevs.com/2020/04/04/comparison-of-different-ev-batteries-in-2020/ (2020)
4. BMW i3 Battery Pack Dimensions. https://www.torqeedo.com/us/en-us/technology-and-environment/battery-technology.html.
5. 2018 Nissan LEAF First Responder's Guide. https://www.nfpa.org/Training-and-Events/By-topic/Alternative-Fuel-Vehicle-Safety-Training/Emergency-Response-Guides/Nissan. (*see* Section 2-1.1 for battery pack specifications).
6. Envison AESC cell specifications. https://www.envision-aesc.com/en/product.html (These cells are used in Nissan Leaf).
7. Product specification of LG-Chem E63 Li-ion pouch cells. *LG Chem* (2018). (These cells are used in Renault ZE40 and Hyundai IONIQ).
8. Specifications of 2020 Renault ZOE ZE50 Batteries. https://www.evspecifications.com/en/comparison/ae0f3bd (2020)
9. Caine J. Battery update: development and testing. *AVL Powertrain UK Ltd*. (November 20, 2019).
10. Sun S.Q., Disassembly Report of Jaguar I-PACE and Tesla Model 3 Battery Packs, *General Power*, Hangzhou, China. (2019)
11. Battery Packs of Modern xEVs-A Comprehensive Engineering Assessment. https://totalbatteryconsulting.com/industry-reports/Battery-packs-report/Extract-from-the-Battery-Pack-Report.pdf *Total Battery Consulting* (2019).
12. BYD Blade prismatic battery cell specs and possibilities. https://pushevs.com/2020/05/26/byd-blade-prismatic-battery-cell-specs-possibilities/ (2020)
13. Wang, C., He, L., Sun, H., Lu, P., Zhu, Y. Battery pack, vehicle and energy storage device. China patent CN110165118B. (2019)
14. Wang, C.Y., Xu, T., Ge, S., Zhang, G., Yang, X.G., Ji, Y. A Fast Rechargeable Lithium-Ion Battery at Subfreezing Temperatures. *J. Electrochem. Soc.* **163**(9)**,** A1944-A1950 (2016).

15. Mastali, M., Foreman, E., Modjtahedi, A., Samadani, E., Amirfazli, A., Farhad, S., *et al.* Electrochemical-thermal modeling and experimental validation of commercial graphite/LiFePO4 pouch lithium-ion batteries. *Int. J. Therm. Sci.* **129,** 218-230 (2018).
16. Mastali, M., Farkhondeh, M., Farhad, S., Fraser, R. A., Fowler, M. Electrochemical Modeling of Commercial LiFePO4and Graphite Electrodes: Kinetic and Transport Properties and Their Temperature Dependence. *J. Electrochem. Soc.* **163**(13)**,** A2803-A2816 (2016).
17. Zhang, Y., Wang, C.Y., Tang, X. Cycling degradation of an automotive LiFePO4 lithium-ion battery. *J. Power Sources* **196**(3)**,** 1513-1520 (2011).
18. Xu, K., Lam, Y., Zhang, S. S., Jow, T. R., Curtis, T. B. Solvation Sheath of Li+ in Nonaqueous Electrolytes and Its Implication of Graphite/Electrolyte Interface Chemistry. *J. Phys. Chem. C* **111**(20)**,** 7411-7421 (2007).
19. Kulova, T. L., Skundin, A. M., Nizhnikovskii, E. A., Fesenko, A. V. Temperature effect on the lithium diffusion rate in graphite. *Russ. J. Electrochem.* **42**(3)**,** 259-262 (2006).
20. Landesfeind, J., Gasteiger, H. A. Temperature and Concentration Dependence of the Ionic Transport Properties of Lithium-Ion Battery Electrolytes. *J. Electrochem. Soc.* **166**(14)**,** A3079-A3097 (2019).
21. Naumann, M., Schimpe, M., Keil, P., Hesse, H. C., Jossen, A. Analysis and modeling of calendar aging of a commercial LiFePO4/graphite cell. *J. Energy Storage* **17,** 153-169 (2018).